Supplementary Information

# Mechanically driven SMR-based NEMS magnetoelectric antennas

Xianfeng Liang [1,*], Huaihao Chen [1,*], Neville Sun [1,*], Elizaveta Golubeva [3], Cai Müller [3], Sushant Mahat [5], Yuyi Wei [1], Cunzheng Dong [1], Mohsen Zaeimbashi [1], Yifan He [1], Yuan Gao [2], Hwaider Lin [2], David G. Cahill [5], Mohan Sanghadasa [6], Jeffrey McCord [3,4] and Nian X. Sun [1,2,**]

[1] Department of Electrical and Computer Engineering, Northeastern University, Boston, MA 02115, USA

[2] Winchester Technologies, LLC, Burlington, MA 01803, USA

[3] Institute for Materials Science, Kiel University, Kiel, 24143, Germany

[4] KiNSIS - Kiel Nano, Surface and Interface Science, Kiel University, Kiel, 24143, Germany

[5] Department of Materials Science and Engineering, Engineering and Materials Research Laboratory, University of Illinois at Urbana-Champaign, Urbana, IL 61801, USA

[6] U.S. Army Combat Capabilities Development Command Aviation & Missile Center, Redstone Arsenal, AL 35898

* Xianfeng Liang, Huaihao Chen and Neville Sun contributed equally to this work.

** Correspondence: n.sun@northeastern.edu; Tel.: +1 (617) 373 3351.

## Thin-film surface qualities and stress states

To characterize the qualities and evaluate the misalignment of magnetic anisotropy of SMR-based ME antenna, the root-mean-square (RMS) surface roughness and biaxial stress of Bragg reflector, piezoelectric and magnetostrictive layers are given in Supplementary Fig. 1. All films were prepared by sputtering as a single layer on Si wafers. The RMS roughness of $SiO_2$, W, ZnO and FeGaB films is 2.39, 2.34, 2.07 and 1.00 nm, respectively as shown in Supplementary Fig. 1a-d. The typical RMS value of polished Si wafers is between 0.1 to 0.5 nm[1], which is much smoother than Bragg reflector and ZnO films deposited in our system. Since the magnetic multilayer is the topmost layer of ME antenna, the rougher substrate impairs the strength of the UMA in patterned devices as revealed in Fig. 2. The high-resolution 2D stress scanning over entire wafer surface is performed by a commercial system named "kSA MOS UltraScan" from k-Space Associates, Inc. The 2D stress scanning results of $SiO_2$, W, ZnO and FeGaB films are presented in Supplementary Fig. 1e-h. By utilizing a 2D laser array, the local curvature of the sample in both X and Y directions can be determined according to changes in the reflected laser array spot spacing at each point. In this way, the quantitative film stress mapping in two dimensions (horizontal (H) stress and vertical (V) stress) is able to be simultaneously generated by determining the curvature pre- and post-deposition of the sample. Although we have improved the condition of films' stress, the optimized quality that stress is nearly zero is not achieved. And as we expected, there is a large and non-uniform stress in X and Y directions for FeGaB film (Supplementary Fig. 1h) that confirms the misalignment of E.A. from in-situ magnetic field direction.

## Acoustic properties and characterizations

The acoustic velocity ($\nu$) data of $SiO_2$, W, ZnO and FeGaB are experimental values that were measured by professor David Cahill's group at University of Illinois and the acoustic impedance values are calculated according to the equation: $Z=\rho\cdot\nu$, where densities $\rho$ were assumed to be same as the values in references. They employ the picosecond acoustic (PA) technique[2, 3] to measure the travel time of strain through the thin-film materials. The details of the pump-probe setup are elaborated in reference [3]. All thin films are deposited on top of Si wafers with Al capping layers. A sub-picosecond pump laser pulse is focused onto the Al surface with a spot diameter of ~20 μm. The pump pulse excites a longitudinal acoustic wave by thermal expansion. Then, the longitudinal acoustic wave travels through different layers of the sample and is partially reflected from each interface in the sample. The reflected echoes are measured by a probe pulse at the sample surface in time domain. The time (t) between echoes is the round-trip time of an acoustic wave to travel through a layer and reflect from a subsequent interface. Thus, the acoustic velocity can be calculated as $v = 2L/t$, where L is the thickness of the layer. The thickness of each sample layer was measured by X-ray reflectivity method. In these materials as listed in Supplementary Table 1, $SiO_2$ and Ir have the lowest and highest acoustic impedance, respectively. Heavy metals, such as Pt, Ir, etc. usually have large acoustic impedance, however, they are expensive materials and not cost-effective. Tungsten (W) is the next best alternative for a high acoustic impedance film but it should be carefully taken into account that the W thin films exhibit very large intrinsic stress during deposition.

As shown in Supplementary Fig. 2 of the PA results for different samples, the echoes expected from the Al layer are marked by vertical black lines while the echoes from the sample layer are marked by vertical blue lines. Using the difference between black lines, the round-trip time for a strain to travel through the Al layer and reflect from the subsequent interface can be measured. Similarly, the round-trip time for the strain to travel through the sample layer and reflect from the subsequent interface can be obtained by the difference between blue lines. The same information can also be achieved from the difference between the first black line and first blue line. The round-trip time for $SiO_2$, ZnO, W, and FeGaB were measured and presented in Supplementary Fig. 2. Accordingly, the acoustic velocities were calculated and shown in Supplementary Table 1.

**1D Mason model calculation results**

The 1D Mason model calculation results for 4 and 5 periods of $SiO_2$/W layers are shown in Supplementary Fig. 3. It is obvious that minimal improvement in the reflection coefficient and operation bandwidth is obtained when the number of periods exceeds three. Therefore, we decided to use three pairs of $SiO_2$/W layers as the Bragg reflector.

**Device fabrication process and SMR device layout**

The fabrication process flow of the proposed SMR ME antenna is shown in Supplementary Fig. 4. A high resistivity (HR) (>10000 Ω·cm) silicon wafer was chosen to start the process (a). The Bragg reflector consisting of three pairs of W (531 nm)/$SiO_2$ (543 nm) layers was deposited on top of HR Si wafer (b). A 50-nm-thick Pt film was sputter-deposited by DC sputtering and patterned by lift-off on top of the Bragg reflector to establish the bottom electrodes (c). Then, the ZnO film was sputter-deposited by RF reactive sputtering and vias were etched by Hydrochloric (HCl) acid to access the bottom electrodes (d). After that, a 100-nm-thick Au film was sputtered and patterned by lift-off to form the top ground electrode (e). Finally, the FeGaB/$SiO_2$ multilayer layer was deposited by a magnetron sputtering and patterned by lift-off (f). Supplementary Fig. 4g shows the 3D schematic drawing of the SMR ME antenna.

**Very-near-field measurements**

The radiating near-field and far-field regions, which are known as Fresnel and Fraunhofer zones, are most frequently measured to characterize antennas. Traditional antenna far-field patterns are characterized by utilizing far-field testing techniques in a shielded chamber or projecting near-field data sets into far-field patterns using Fourier transform algorithms[9-11]. A controlled and shielded environment provided by anechoic chambers is required to exclude the interference of external reflections and noise, therefore, accurate far-field patterns are acquired. To perform accurate antenna testing, a large physical space with radio wave foam and a precise three-axis positioner are needed. Furthermore, projection errors can be generated on account of the coupling between AUTs and near-field sensors. The required number of sampling points and shielded chamber can prove to be a costly and slow method for antenna testing. Recently, a novel near-field technology was developed to overcome these challenges. The EMSCAN RFxpert utilizes a probe array system to measure near-field results and accurately calculated into far-field patterns. On the contrary to traditional measurement techniques, the very-near-field method measures antenna under test (AUT) in the reactive region, where the sensors are close enough to influence the AUT's performance.

As shown in Supplementary Fig. 5, the very-near-field results of SMR antenna at 1.75 GHz were then measured and transformed to the far-field pattern using well-established algorithms. The very-near magnetic field pattern of SMR ME antenna was measured by EMSCAN RFxpert array system and displayed in Supplementary Fig. 5a. To eliminate the coupling effects of the probe array, a second algorithm was employed to adjust the far-field transformation. The transformed far-field radiation pattern is presented in Supplementary Fig. 5b, in which the maximum realized gain of -19.6 dBi is obtained. This value is consistent with the results measured in chamber as shown in Fig. 4a.

## References


1. Teichert C, MacKay J, Savage D, Lagally M, Brohl M, Wagner P. Comparison of surface roughness of polished silicon wafers measured by light scattering topography, soft-x-ray scattering, and atomic-force microscopy. *Applied physics letters* 1995, **66**(18)**:** 2346-2348.

2. Grahn HT, Maris HJ, Tauc J. Picosecond ultrasonics. *IEEE Journal of Quantum Electronics* 1989, **25**(12)**:** 2562-2569.

3. Kang K, Koh YK, Chiritescu C, Zheng X, Cahill DG. Two-tint pump-probe measurements using a femtosecond laser oscillator and sharp-edged optical filters. *Review of Scientific Instruments* 2008, **79**(11)**:** 114901.

4. Villa-López FH, Rughoobur G, Thomas S, Flewitt AJ, Cole M, Gardner JW. Design and modelling of solidly mounted resonators for low-cost particle sensing. *Measurement Science and Technology* 2015, **27**(2)**:** 025101.

5. Chung C-J, Chen Y-C, Cheng C-C, Wei C-L, Kao K-S. Influence of surface roughness of Bragg reflectors on resonance characteristics of solidly-mounted resonators. *ieee transactions on ultrasonics, ferroelectrics, and frequency control* 2007, **54**(4)**:** 802-808.

6. Lanz R, Muralt P. Bandpass filters for 8 GHz using solidly mounted bulk acoustic wave resonators. *IEEE transactions on ultrasonics, ferroelectrics, and frequency control* 2005, **52**(6)**:** 938-948.

7. Olivares J, Wegmann E, Capilla J, Iborra E, Clement M, Vergara L*, et al.* Sputtered SiO 2 as low acoustic impedance material for Bragg mirror fabrication in BAW resonators. 2009 IEEE International Frequency Control Symposium Joint with the 22nd European Frequency and Time forum; 2009: IEEE; 2009. p. 316-321.

8. Tanskaya T, Zima V, Kozlov A. The influence of surface roughness of Bragg reflector layers on characteristics of microwave solidly mounted resonator. 2015 International Siberian Conference on Control and Communications (SIBCON); 2015: IEEE; 2015. p. 1-4.

9. Johnson RC, Ecker HA, Hollis JS. Determination of far-field antenna patterns from near-field measurements. *Proceedings of the IEEE* 1973, **61**(12)**:** 1668-1694.

10. Yaghjian A. An overview of near-field antenna measurements. *IEEE Transactions on antennas and propagation* 1986, **34**(1)**:** 30-45.

11. Evans GE. Antenna measurement techniques. *ah* 1990.

**Figures and tables**

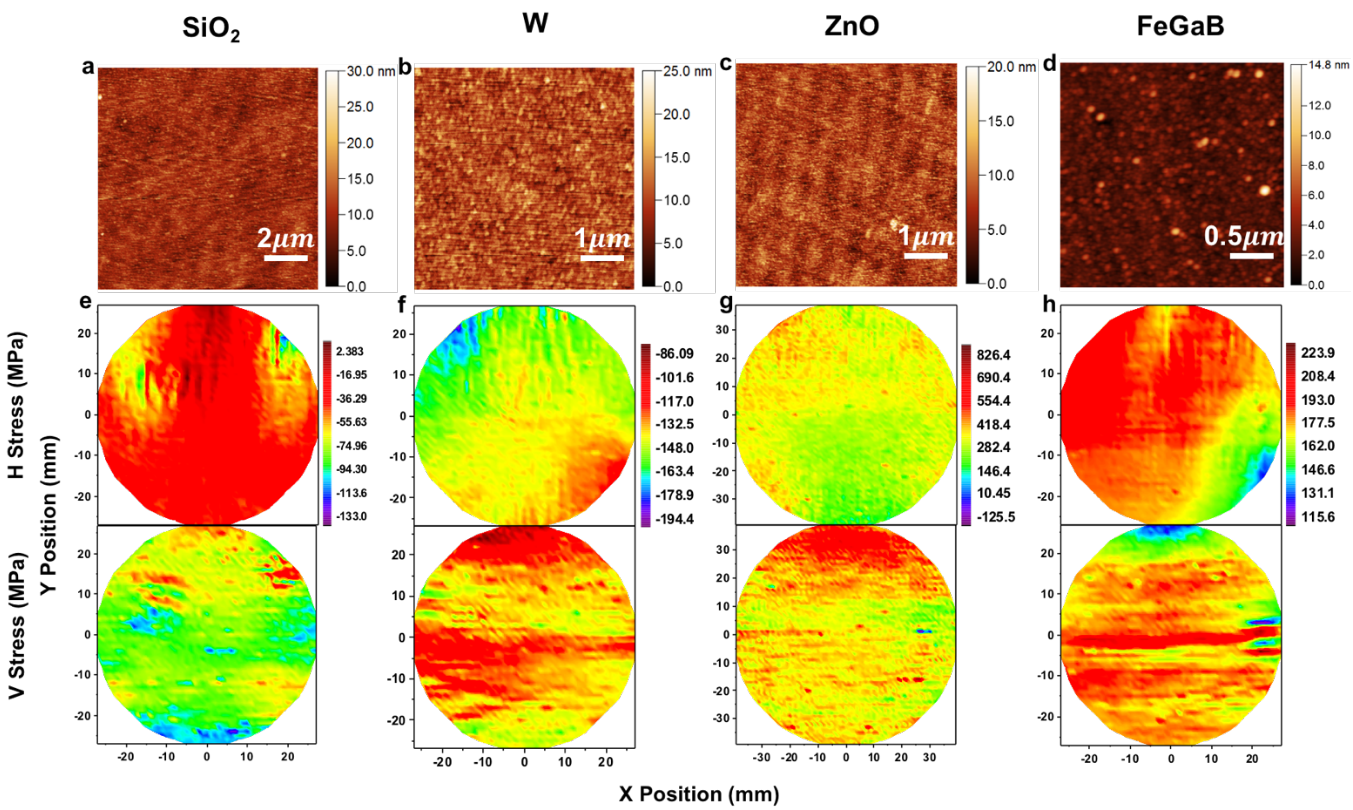


**Supplementary Figure 1. AFM and stress images of materials for SMR-based ME antennas. a-d,** AFM images of $SiO_2$ (**a**), W (**b**), ZnO (**c**) and FeGaB (**d**). **e-h,** Stress scanning results of $SiO_2$ (**e**), W (**f**), ZnO (**g**) and FeGaB (**h**). First row: horizontal (H) stress that is parallel to X axis; second row: vertical (V) stress that is parallel to Y axis. All samples were prepared on Si wafer.

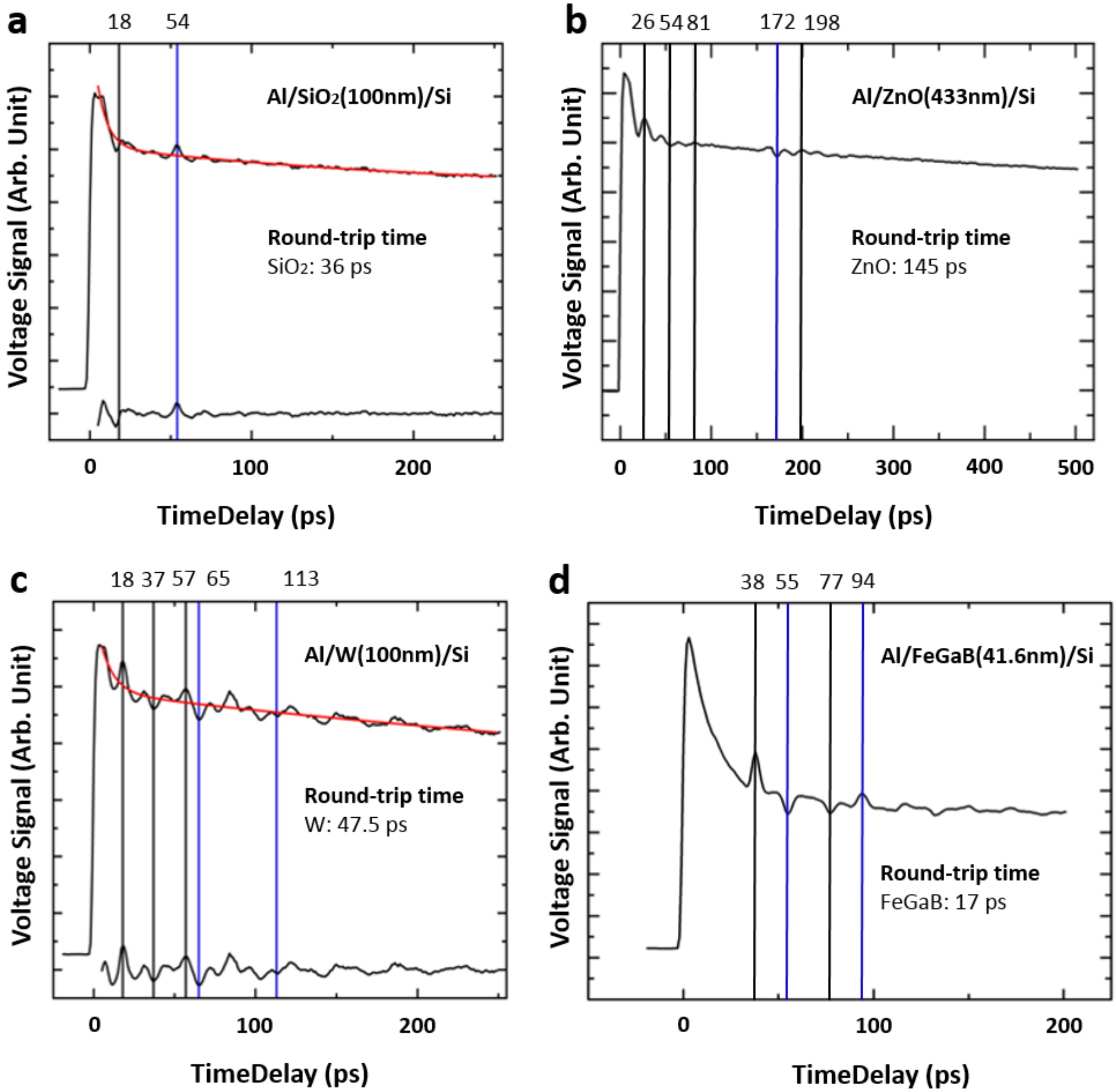


**Supplementary Figure 2. Picosecond acoustics (PA) for longitudinal acoustic wave echo measurements of different thin-film materials. a,** $SiO_2$. **b,** ZnO. **c,** W. **d,** FeGaB. The layer structures and round-trip time for sample materials are shown in the figure. Si is the silicon substrate. Vertical black lines indicate the echoes from Al layer and vertical blue lines indicate the echoes from sample layer.

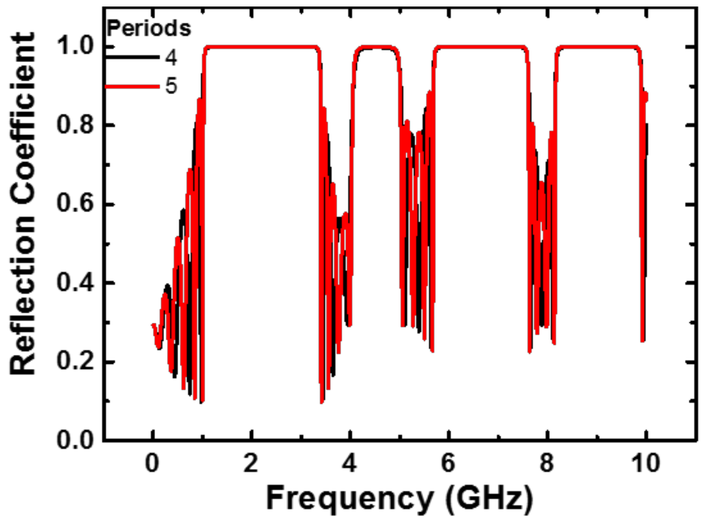


**Supplementary Figure 3. 1D Mason model calculation.** The reflection coefficient of the designed Bragg reflector consisting of 4 and 5 pairs of $SiO_2$/W layers.

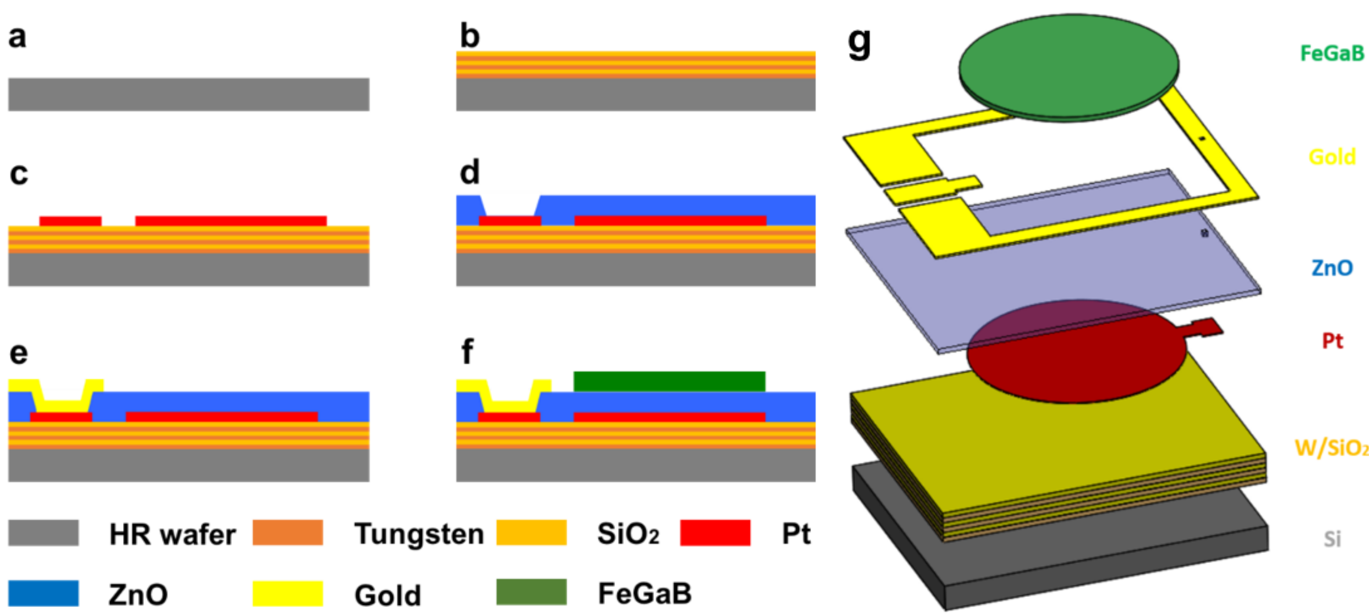


**Supplementary Figure 4. Fabrication process flow of the designed SMR-based ME antenna. a,** Process flow of the proposed ME antenna. Start with HR Si wafer. **b,** Bragg reflector deposition. **c,** Bottom electrode Pt thin film deposition and patterning. **d,** Piezoelectric layer ZnO deposition and wet etch of vias. **e,** Top electrode Au deposition and patterning. **f,** Magnetic multilayer FeGaB/$SiO_2$ deposition and patterning. **g,** 3D schematic drawing of the ME antenna.

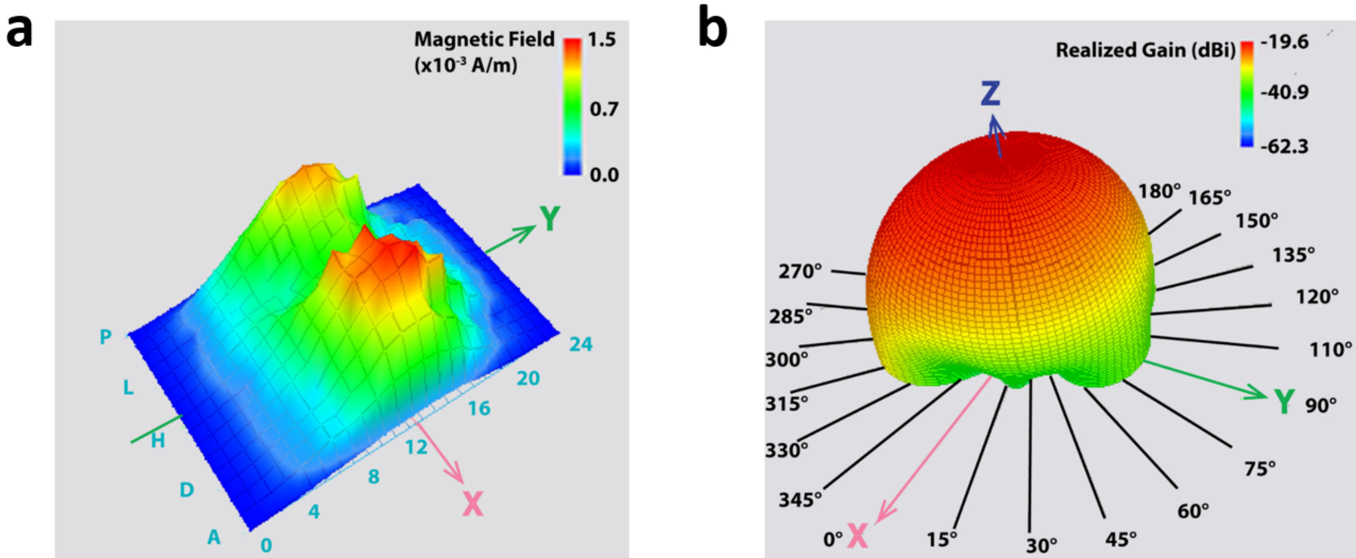


**Supplementary Figure 5. Very-near-field measurements of SMR antenna. a,** Very-near magnetic field pattern measured by EMSCAN RFxpert. **b,** Far-field radiation pattern calculated from the very-near-field results. The maximum realized gain is -19.6 dBi.

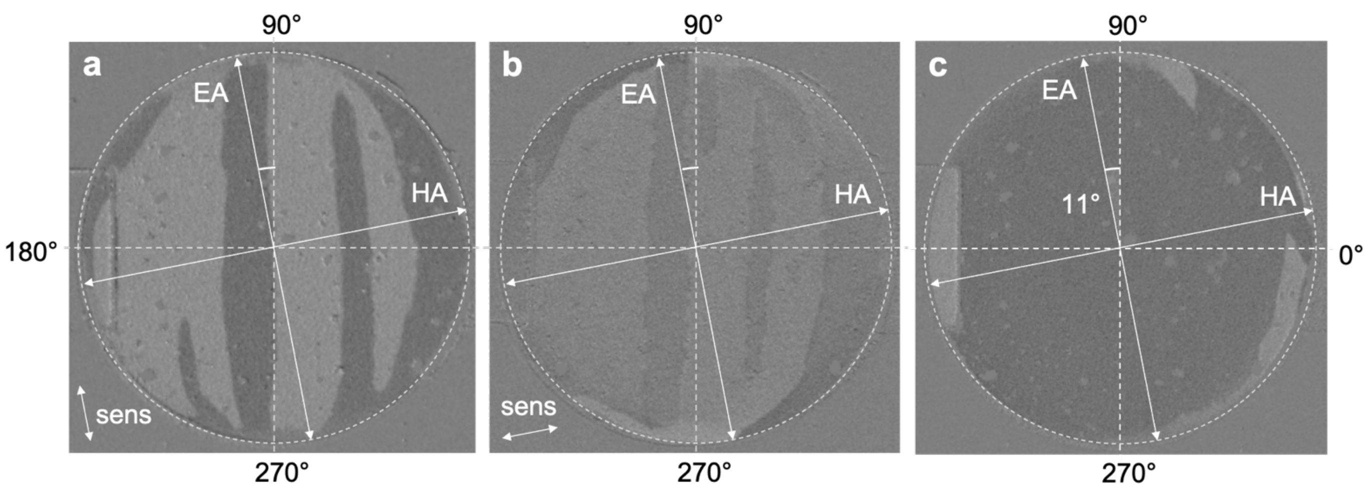


**Supplementary Figure 6. Magnetooptical images of SMR-based ME antennas. a-b,** Demagnetized state with decaying magnetic field applied along the hard axis of the sample (11-degree axis). MOKE sensitivity is along the 101° (E.A.) (**a**) and 11° (H.A.) (**b**) axis. **c,** Remanent state after decaying ac magnetic field application along the easy axis of the sample (101-degree axis). MOKE sensitivity is along the 101° (E.A.) axis.

Supplementary Table 1. Acoustic Properties of Materials used in Bragg Reflector.

| **Acoustic Properties** | **Materials** | **Acoustic Velocity ($m.s^{-1}$)** | **Acoustic Impedance ($x10^6$ $kg.m^{-2}.s^{-1}$)** | **Device Thickness (nm)** | **Reference** |
|---|---|---|---|---|---|
| **Low Impedance** | Al | 6450 | 17.4 | / | [4] |
| | AlN | 10400 | 34.0 | / | [5] |
| | Si | 8433 | 19.6 | / | [6] |
| | $SiO_2$ | 5450 | 12.0 | / | [7] |
| | | 5600 | 12.1 | 543 | This work |
| | Ti | 6071 | 27.3 | / | [5] |
| | ZnO | 6330 | 36.0 | / | [8] |
| | | 5970 | 34.0 | 605 | This work |
| **High Impedance** | Au | 3430 | 66.2 | / | [4] |
| | Ir | 5350 | 120 | / | [8] |
| | Mo | 6280 | 64.1 | / | [4] |
| | Pt | 4230 | 90.9 | 50 | [6] |
| | W | 5230 | 101.0 | / | [8] |
| | | 4200 | 81.1 | 531 | This work |
| **Magnetostrictive** | FeGaB | 4890 | 28.4 | 900 | This work |